GENERAL PHYSICS

I. MOLECULE MICROSCOPY

Academic and Research Staff

Prof. John G. King
Dr. Augustine Chong
Dr. John W. Peterson
Dr. Stanley R. Rosenthal
Dr. James C. Weaver

Graduate Students

H. Frederick Dylla
Joseph A. Jarrell
Dusan G. Lysy
Bruce R. Silver
Peter W. Stephens

A. PROTOTYPE SCANNING DESORPTION MOLECULE MICROSCOPE (SDMM)

JSEP

Joint Services Electronics Program (Contract DAAB07-74-C-0630)
National Institutes of Health (Grant 5 PO1 HL14322-04)

H. Frederick Dylla

A prototype scanning desorption molecule microscope[1] based on the process of electron stimulated desorption[2] has been constructed and tested. The instrument is capable of mapping the spatial variation of adsorbed atoms and molecules on solid surfaces. The instrument has been designed as a general tool for surface science studies by including Auger electron spectrometry, instrumentation for the measurement of angular and energy distribution of desorbed ions and neutrals, and facilities for producing atomically clean surfaces and for adsorbing controlled quantities of pure gases. Initial observations show the variations of physically adsorbed gases on a Si-Au test sample. These serve to illustrate the instrumental sensitivity and surface specificity.

The experimental apparatus is contained in a stainless-steel, copper-gasketed ultrahigh vacuum chamber (see Fig. I-1). The chamber is pumped by a liquid-nitrogen-trapped, 10-cm diffusion pump and a titanium sublimation pump through the ports labeled (P). Base pressures of $1 \cdot 10^{-10}$ Torr are obtained after a 250°C bakeout. The sample (S) is mounted on a manipulator from the top of the chamber with provisions for heating, cooling, and temperature measurement. At the midplane of the chamber circumferential ports house the instrumentation. The electron beam system (EBS), described in Section II-A, produces a beam of electrons of variable energy, spot size, and current that can be scanned across the sample. The electron gun (EG) of the EBS is a Braucks-Steigerwald gun design with either a tungsten hairpin or Schottky filament as a source. Following the gun is a pair of electrostatic lenses, the condenser (CON), and objective (OBJ) which focus the electron beam to a minimum diameter of 3-5 μm. Not shown are pairs of deflection plates for alignment, rastering, and modulation of the beam. An Auger electron spectrometer (AES) manufactured by Physical Electronics Industries, Inc., Eden Prairie, Minnesota, is positioned 78° from the EBS axis. Secondary electrons scattered from the sample are energy analyzed by a cylindrical mirror

JSEP

JSEP

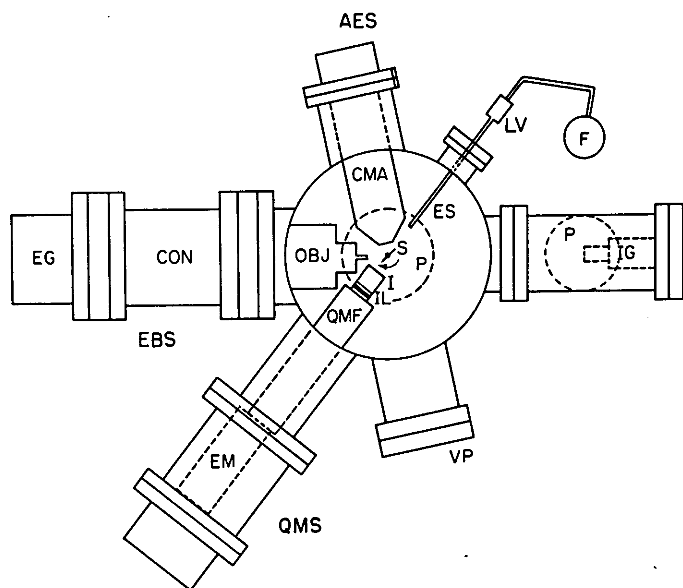

Fig. I-1. Prototype scanning desorption molecule microscope (SDMM).

analyzer (CMA) and detected by a CuBe electron multiplier (not shown). Electronic differentiation of the CMA signal allows the small Auger electron signals to be distinguished from the large background of backscattered electrons. Measurements of scattered electrons near the energy of the incident electron beam allow collection of data on the characteristic energy losses from the sample surface. A quadrupole mass spectrometer (QMS), manufactured by Extranuclear Laboratories, Inc., Pittsburgh, is positioned 52° from the EBS axis. Neutral atoms and molecules desorbed from the sample by the electron beam are ionized by an efficient (.1%) electron bombardment ionizer (I), extracted and focused by a system of ion lenses (IL), mass analyzed by a quadrupole mass filter (QMF) and detected with an electron multiplier (EM). Ions desorbed from the sample can be focused by the ion lenses with the ionizer potentials set to zero. The electron multiplier signal from the QMS is measured with a wide bandwidth (3-300 kHz) electrometer or by a 10-MHz pulse amplifier and count-rate meter, depending on the signal magnitude. If the signal-to-noise ratio is low, the signal is further conditioned with a lock-in amplifier referenced to the electron beam modulation. Energy distribution of desorbed ions and neutrals is obtained by pulsing the electron beam (typically for 1 μs) and measuring the resulting time-of-flight distribution through the QMS.

An effusive molecular beam source (ES) is placed 2.5 cm from the sample to dose the sample surface with controlled amounts of pure gases from 1-liter glass flasks (F) through a precision leak valve (LV). The remaining circumferential ports contain a sputter ion gun (IG), to clean the sample surface by low-energy (.1-1 kV) rare-gas ion bombardment, and a view-port (VP). Not shown are several small ports for a

JSEP

gas-handling manifold, a nude Bayard-Alpert ionization gauge, and a sorption pump.

Any of the signals stimulated by the electron beam, i. e., desorbed neutrals or ions, backscattered secondary or Auger electrons, or the absorbed electron current in the sample, can be amplified and applied to the control grid of a cathode ray tube (CRT) driven in synchronism with the electron beam as it is scanned across the sample. The resulting micrographs yield the spatial variation of secondary electron emission in the case of the absorbed current or secondary electron micrographs (SEM), the spatial variations in elemental composition within the first few atomic layers of the sample when scanning Auger micrographs (SAM) are obtained, and the spatial variation of atomic and molecular adsorption as determined by scanning electron stimulated desorption micrographs (SDM). Geometric considerations in the design of the apparatus prohibit obtaining all three types of micrographs simultaneously, but absorbed current micrographs can be obtained simultaneously with Auger micrographs or with desorption micrographs, and SAMs can follow SDMs consecutively in a minimal time so that no change in surface conditions has occurred. In actual practice two display CRTs are used simultaneously; a storage CRT for adjustment of image contrast, magnification, etc., and a higher resolution, less persistent CRT for photographing the micrographs.

Figures I-2 and I-3 show a set of micrographs obtained in an initial test of the apparatus. Two silicon crystals were prepared as test samples. A rectangular array of gold spots was evaporated onto the polished Si surfaces through two different-sized stainless-steel meshes, yielding an array of approximately 250 μm spots on one crystal and 100 μm spots on the second crystal. On both crystals the Au thickness was approximately 100 Å as determined by a quartz film thickness monitor during the evaporation process.

Figure I-2a shows an SEM of the Si sample with the 250 μm spots. The micrograph, taken with the absorbed electron current as a 3.0 kV, 1 μA beam was scanned across the sample, and shows the variation in surface conductivity and secondary electron emission. In this mode the Si areas with a higher secondary emission coefficient appear brighter (more positive) than the darker (more negative) Au spots. Figure I-2b shows a region of Fig. I-2a that was magnified by 7.5 by decreasing the raster dimensions by this factor. The electron beam spot size at the sample is estimated from these micrographs to be of the order of 25 μm. At present, the EBS is operating with no limiting aperture preceding the condenser or objective lenses.

Figure I-4 shows an Auger electron spectrum of the Si/Au (100 μm) sample after a brief heat treatment (700°C for 5 min) in a residual gas pressure of $4 \cdot 10^{-8}$ Torr (primarily CO, H_2, H_2O). As well as primary Si and Au peaks, the 272 V carbon peak and 475-510 V oxygen triplet are also present. Figure I-2c and 2d shows scanning Auger micrographs of the same sample taken immediately after the spectrum of Fig. I-4. Figure I-2c is an SAM produced by the intensity variation of the 69 eV Au peak, and

JSEP

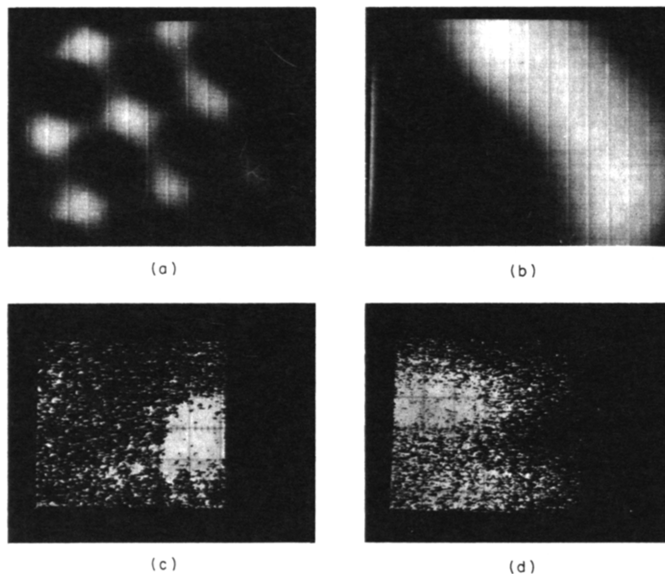

Fig. I-2. (a) SEM of Si crystal with an overlayer of 250 μm Au spots (dark).
(b) SEM of the sample imaged in (a) with 7.5 magnification.
(c) SAM of Si crystal with an overlayer of 100 μm Au spot imaged with Au (69 eV) Auger electrons.
(d) SAM of the sample imaged in (c), imaged with O (510 eV) Auger electrons.

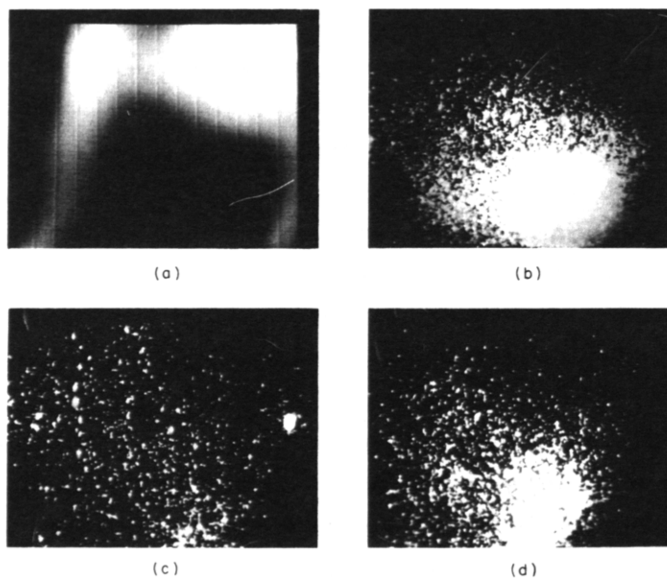

Fig. 1-3. (a) SEM of a portion of Si crystal with an overlayer of 100 μm Au spots (poorly resolved; dark area is Au).
(b) SDM of the sample area shown in (a) imaged with desorbing CO^+ ions.
(c) SDM imaged with CO^+ ions after sample was briefly heated to 730°C.
(d) SDM imaged with CO^+ ions 20 min after (c), showing readsorption of CO on the Au surface.

JSEP

JSEP

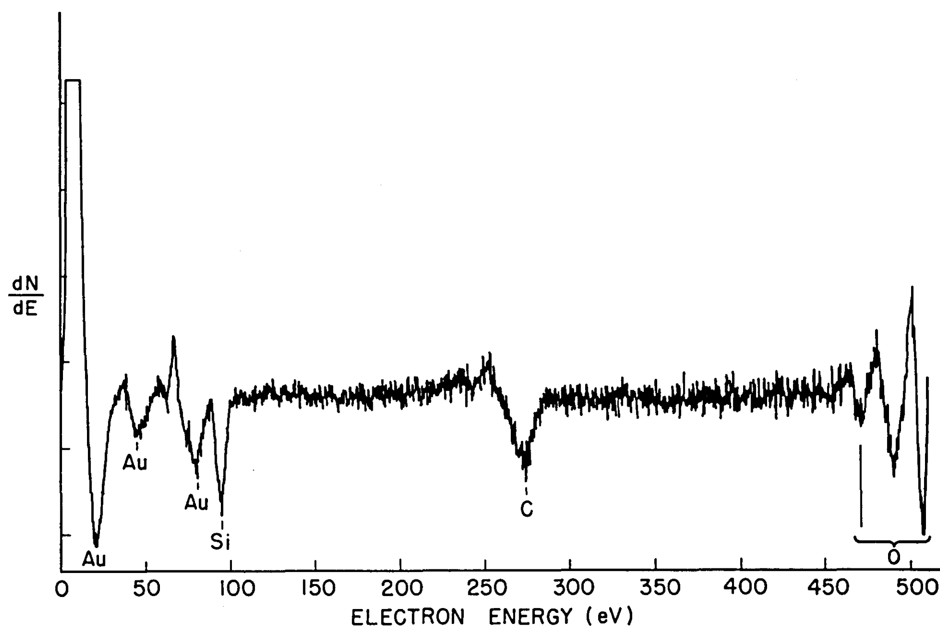

Fig. I-4. Auger electron spectrum (0-500 eV) of Si/Au (100 μm) sample (3.5 kV, .2 μA incident electron beam).

Fig. I-2d is an SAM of the same area produced by the 510 V O peak. In both cases the micrographs were produced by a 1500 V, .8 μA beam scanned across an approximate area of 200 μm × 200 μm. The interesting feature of the micrographs is the predominance of the oxygen Auger signal on the silicon regions of the sample, which very likely indicates the presence of chemisorbed oxygen or oxygen containing molecules (CO, H_2O, etc.) on the silicon.

Figure I-5 shows a typical ESD ion mass spectrum of the Si/Au (100 μm) sample obtained with an incident 1500 V, .3 μA beam. Figure I-2c and 2d shows a sequence of SDMs produced by the intensity variations of the ionic desorption signals. Figure I-3a is a simultaneous SEM of the area of the sample that is being scanned (the dark area is Au). Figure I-3b is an SDM produced by desorbing CO^+ ions, and by comparison with the SEM (Fig. I-3a) the CO^+ signal is seen to predominate on the Au regions of the sample. Figure I-3c shows an SDM of the same area with the sample at a temperature of 730° C; the CO^+ surface signal has been significantly reduced. Figure I-3d is an SDM of the same area 20 min after the sample was allowed to cool in a partial pressure of CO of $2 \cdot 10^{-8}$ Torr, and the CO^+ surface signal has been substantially increased by readsorption onto the Au surface. The total pressure ($P = 4 \cdot 10^{-8}$ Torr) and residual gas composition were identical for both SAM and SDM measurements. Similar micrographs have been obtained for H_2^+, which show H_2 coadsorbed with the CO on the Au surfaces.

JSEP

JSEP

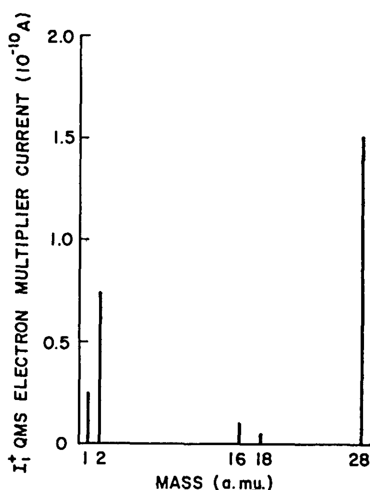

Fig. I-5.
ESD ion mass spectrum (0-30 amu) from Si/Au (100 μm) sample (1.5 kV, .3 μA incident electron beam).

A preliminary interpretation of the surface conditions of the Si/Au samples based on these micrographs is as follows: Residual gases in the vacuum system, primarily CO and H_2, are physisorbed on the Au surfaces. These same residual gases are chemisorbed to Si, with chemisorbed CO contributing to C and O Auger signals, in addition to the contributions of chemisorbed O_2, O, and H_2O to O Auger signal. There is evidence that CO chemisorbs on Si with an anomalously low saturation coverage,[3,4] whereas O_2 and H_2O will saturate at a full monolayer coverage corresponding to one adsorbed molecule per pair of substrate Si atoms.[3] The oxygen SAM (Fig. I-2d) is evidently most sensitive to the chemisorbed oxygen-containing molecules, showing a strong O Auger intensity only on the silicon surfaces. In comparison, the SDMs are most sensitive to the physisorbed gases on the chemically inert Au surfaces. This observation is consistent with the generally observed trend that ESD cross sections are larger for adsorbates with smaller binding energies.[5] We hope to exploit this sensitivity to the presence of weakly bound adsorbates to make the SDMM a useful tool for mapping surface chemical potentials.

An order-of-magnitude calculation on the expected signal strength for the micrographs in Fig. I-3 will estimate the efficiency of the process, the change in surface conditions during the "exposure," and account for the spotty nature of the photographs. The electron beam raster is an array of 256 × 256 points generated by two digital ramp generators. For the SDMs shown in Fig. I-3, this array of 65,000 points covers an area of the sample approximately 500 μm on a side and is scanned in a total time of 5 minutes. Therefore, a time $\Delta t = 300\ s/6.5 \cdot 10^4 \approx 5 \cdot 10^{-3}$ s is spent on each grid point. The detected desorption signal (CO^+) is $\sim 1 \times 10^{-15}$ A before the electron multiplier or roughly $5 \cdot 10^3$ CO^+ ions per second, or ~25 per Δt. The shot noise inherent in a signal of such small magnitude accounts for the choppy appearance of the micrographs.

A crude estimate can be made of the total number of ions desorbed by the incident electron beam compared with the detected signal, to evaluate the efficiency of the detection scheme. The detected signal originates from an irradiated area, A, of the sample at each grid point, which we have found[2] to be approximately 25 μm. If a full monolayer

JSEP

JSEP

coverage of CO is assumed, then the number of CO molecules per area A is $n_m = (2.5 \cdot 10^{-3}\ \text{cm})^2 \cdot 10^{15}\ \text{cm}^{-2} = 6 \cdot 10^9$. The number of desorbed ions per Δt from this total initial coverage is $\Delta n = n_e Q^+ n_m$, where n_e is the number of incident electrons per Δt per A, and Q^+ is the electron stimulated desorption (ESD) ionic cross section.

ESD ionic cross sections have been measured for only a few adsorbate-adsorbent systems, since the surface coverage, electron current density, and ion collection efficiency all have to be known. Two such systems in which cross-section measurements have been made are CO/W (Menzel and Gomer[5]) and O_2/Mo (Redhead[6]). Figure I-6 is a plot of measured total ESD cross sections vs binding energy of the adsorbate as determined by flash desorption. Extrapolations of this plot for binding states with physisorption energies (~.1 eV) yield an ESD total cross section of the order of 10^{-16}cm^2.

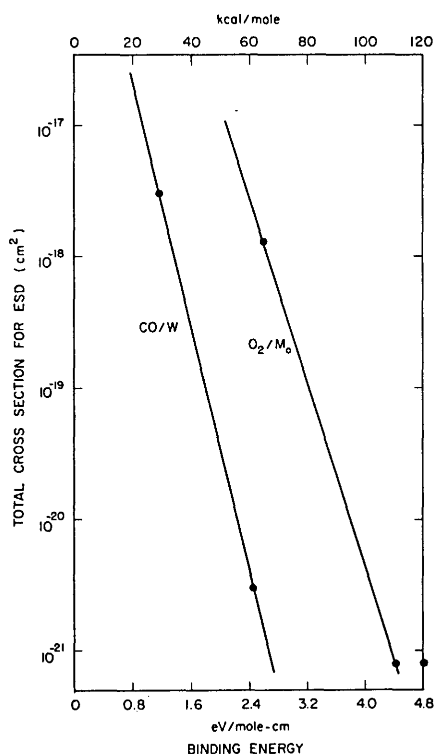

Fig. I-6

ESD cross section vs binding energy for CO on W and O_2 on Mo.

Typically ESD ionic cross sections are 10^{-2}-10^{-4} of the total cross section because of the efficiency of Auger neutralization of ions produced near a metal or semiconductor surface.[7] Estimating a value Q^+ of $10^{-19}\ \text{cm}^2$ for physisorbed CO on Au yields the following number of desorbed ions per Δt per A: $\frac{\Delta n}{A\Delta t} \approx 5$. Therefore the number of detected ions is roughly equal to the number of desorbed ions and the estimated collection efficiency for ions is between 10% and 100%. The total number of desorbed neutrals and ions per area A is of the order of 10^4, which is a small fraction of the $6 \cdot 10^9$ available from

JSEP

JSEP A; therefore, the process of taking a micrograph does not significantly affect the surface coverage in this instance.

In order to understand more fully the surface properties of silicon and the correlation of ESD observations with surface properties, we have begun investigation of the adsorption of simple gases (H_2, H_2O, O_2, CO) on single-crystal Si surfaces, using the apparatus in the prototype SDMM. We are hopeful that the study of the surface properties of a comparatively simple substance will aid in the development of the SDMM. Some preliminary data on the Si(111) surface can be presented.

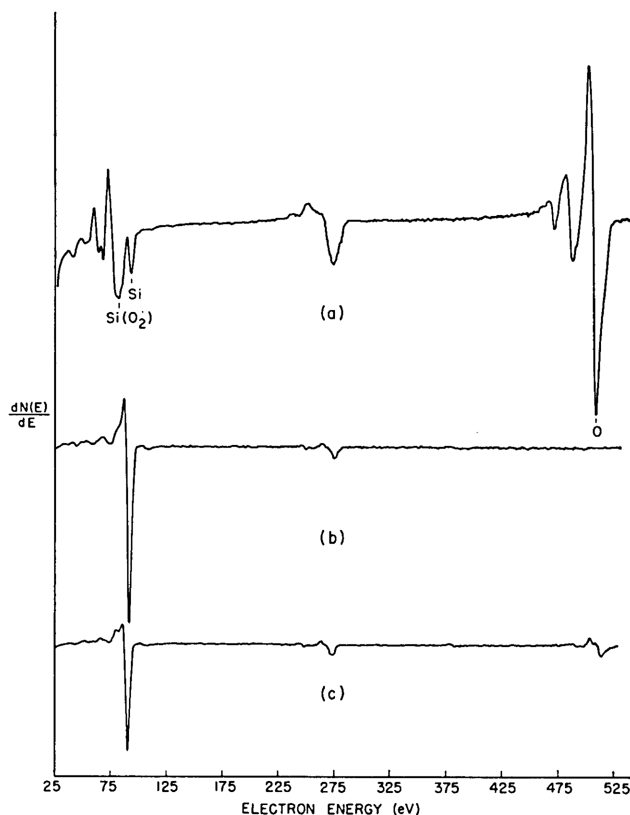

Fig. I-7. (a) Auger electron spectrum of Si(111) crystal prior to surface cleaning. (3.0 kV, 5 μA incident electron beam).
(b) AES of Si(111) after heating for 2 min to 850° C in 10^{-6} Torr O_2.
(c) AES of Si(111) after adsorption of a monolayer of O_2.

Figure 1-7a shows an Auger spectrum of a Si(111) crystal surface before in situ surface cleaning. A substantial oxide layer is evident from the large oxygen triplet peaks (475 eV, 490 eV, 510 eV), the comparatively small primary Si peak (92 eV), and the presence of a substantial 78 eV peak which represents a chemical shift of the primary Si peak because of its oxidized valence state.[8] Substantial surface carbon is also JSEP evident (272 eV). Figure I-7b shows the Auger spectrum of the Si(111) crystal after

JSEP

it has been heated to 850° K in 10^{-6} Torr O_2 for 2 min and then briefly heated to the same temperature in ultrahigh vacuum. The features of the surface oxide have been removed from the spectrum, leaving a strong primary Si peak (92 eV) and a small residual C (272 eV) signal. Figure I-7c shows the spectrum of the clean Si(111) surface after the adsorption of a monolayer of O_2. Note the reappearance of oxygen peaks and a decrease in the magnitude of the primary Si peak.

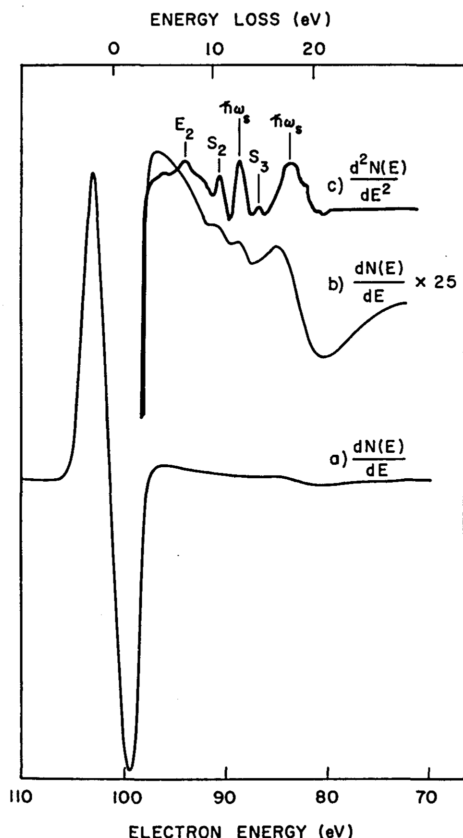

Fig. I-8.

Energy loss spectra of Si(111) surface (incident 101 V, .61 μA electron beam).
Curve a: Differential energy spectrum (-dN(E)/dE) of the elastic peak.
Curve b: Characteristic loss region of the differential spectrum increased in sensitivity by a factor of 25.
Curve c: $-\frac{d^2N(E)}{dE^2}$ spectrum of the loss region with loss peaks identified.

Surface electronic properties of the clean Si(111) surface are evident in the energy loss spectra (Fig. I-8) taken with an incident 100 V electron beam. Figure I-8 (curve a) shows the negative differential energy spectrum $\left(-\frac{dN(E)}{dE}\right)$ of the elastic peak to allow determination of the energy of the incident electrons. Figure I-8 (curve b) shows the characteristic energy loss region of the differential spectrum at an increased sensitivity (× 25). Figure I-8 (curve c) shows the same region of this spectrum doubly differentiated to correlate the loss peak positions with the undifferentiated spectrum. The identified peaks are in agreement with the data of Ibach and Rowe[9] for the Si(111) surface ($\hbar\omega_p$ is the bulk plasmon loss, $\hbar\omega_s$ is the surface plasmon loss, S_2 and S_3 correspond to surface-state transitions, and E_2 is a bulk transition).

JSEP

JSEP

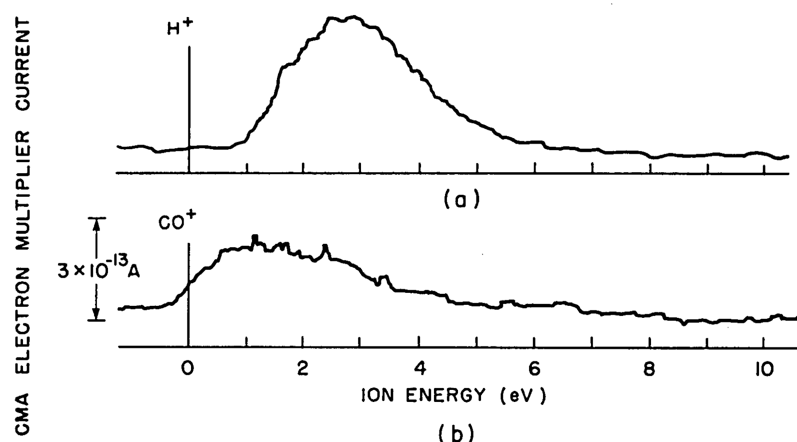

Fig. I-9. ESD ion energy distributions from Si(111) (100 V, 1 μA incident electron beam).
(a) H^+ from chemisorbed H_2O on Si.
(b) CO^+ from chemisorbed CO on Si.

Information concerning adsorbate-adsorbent interaction potentials can be obtained from the energy distribution of ions and neutrals desorbed by electron impact. Ion energy distributions (IED) from the Si(111) surface have been obtained by appropriate changes in the biasing of the cylindrical mirror analyzer (CMA) used for the previous electron spectroscopy. Figure I-9a shows the energy distribution of H^+ ions desorbed by electron impact of chemisorbed H_2O on the Si. Figure I-9b shows the energy distribution of CO^+ ions from chemisorbed CO on the same surface. Since the CMA is sensitive only to the energy and not to the mass of the analyzed particles, the ions were identified by rotation of the crystal so that a fraction of the desorbing ions was collected by the mass spectrometer. The energy scales of the IEDs are uncorrected for the contact-potential difference between the Si and the analyzer (of the order of .1 eV). The substantial differences in peak energy for the desorbing H^+ and CO^+ ions can be related to differences in the H-Si, CO-Si interaction potentials. Detailed analysis of the preliminary data will proceed as more data are collected.

References

1. J. C. Weaver and J. G. King, Proc. Nat. Acad. Sci. USA 70, 2781 (1973).
2. H. F. Dylla and G. A. Herzlinger, Quarterly Progress Report No. 108, Research Laboratory of Electronics, M. I. T., January 15, 1973, pp. 2-5.
3. A. H. Boonstra, Philips Res. Repts. Suppl. No. 3, 1968.
4. B. A. Joyce and J. H. Neave, Surface Sci. 34, 401 (1973).
5. D. Menzel and R. Gomer, J. Chem. Phys. 41, 3329 (1964).

JSEP

6. P. A. Redhead, Can. J. Phys. 42, 886 (1964).
7. H. D. Hagstrum, Phys. Rev. 96, 336 (1954); 119, 940 (1960).
8. C. C. Chang, in P. F. Kane and G. B. Larrabee (Eds.), Characterization of Solid Surfaces (Plenum Press, New York, 1974), pp. 509-575.
9. H. Ibach and J. E. Rowe, Phys. Rev. B9, 1951 (1974).

JSEP

B. LOCALIZED THERMAL DESORPTION BY ELECTRON-BEAM HEATING

Joint Services Electronics Program (Contract DAAB07-74-C-0630)

Bruce R. Silver

1. Spot-Heat Calculation

A crucial parameter in the theory of scanning desorption molecule microscopy (SDMM) is the achievable temperature rise at the surface of a thin sample continuously irradiated by a narrow electron beam.[1] In the geometry of Fig. I-10 uniform energy dissipation $\dot{Q}$ per unit volume over a cylindrical region of radius R and depth h in a slab of thickness L is assumed. The slab has thermal conductivity κ, density ρ, and specific heat C, independent of temperature. The temperature at z = 0 is clamped to some value T_o, and no heat flows across the boundary at z = L.

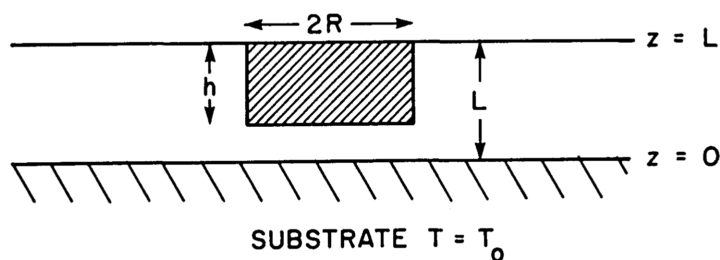

Fig. I-10. Spot-heat geometry: uniform energy deposition in shaded volume.

The Green's function for the temperature rise at $(\vec{r}, t)$ due to an instantaneous pulse of magnitude $\dot{Q}$ at $(\vec{r}', t')$ which satisfies the boundary conditions[2] is

$$T_G(\vec{r}, t, \vec{r}', t') = \frac{\dot{Q}}{\rho C} \cdot \frac{1}{4\pi a L} \cdot \frac{e^{-\frac{s^2}{4a(t-t')}}}{t-t'} \sum_{m=1}^{\infty} e^{-\frac{m^2\pi^2 a(t-t')}{4L^2}} \sin\frac{m\pi z}{2L} \sin\frac{m\pi z'}{2L}, \tag{1}$$

JSEP

JSEP where $s^2 = r^2 + r'^2 - 2rr' \cos \theta'$ and $\alpha = \kappa/\rho C$ is the thermal diffusivity.

By integrating over a finite pulse duration dt' and the source volume $d^3\vec{r}'$, the surface temperature at radius r at time t is given by

$$\Delta T(r,t) = \frac{\dot{Q}}{\pi\kappa} \int_0^{4\alpha t} \frac{dq}{q} \int_0^R dr'\, r' \exp -(r^2+r'^2)/q \; I_o\left(\frac{2rr'}{q}\right) \sum_{m=1,3,5\ldots} \frac{e^{-a_m^2 q}}{m} \sin \frac{m\pi h}{2L}, \tag{2}$$

where $a_m^2 = \frac{m^2\pi^2}{16L^2}$, and I_o is the zero-order modified Bessel function. For values of t comparable to characteristic thermal diffusion times in the irradiation region, the integral becomes messy and must be done numerically. Usually, however, it will be advantageous to use pulse durations much longer than characteristic diffusion times, so that a steady condition described by $t \to \infty$ is approached asymptotically. In that case, the resulting time integral from zero to infinity may be done analytically,[3]

$$T_\infty(r) = \frac{2\dot{Q}}{\pi\kappa} \sum_{m=1,3,5\ldots} \frac{\sin (m\pi h)/2L}{m} \int_0^R dr'r' \cdot \begin{cases} 2I_o(2a_m r')\, K_o(2a_m r), & r' < r \\ 2I_o(2a_m r)\, K_o(2a_m r'), & r' > r \end{cases} \tag{3}$$

where K_o is the zero-order modified Hankel function. Using properties of I and K:

$$\int_0^x z I_o(z)\, dz = x I_1(x) \tag{4a}$$

$$\int_0^x z K_o(z)\, dz = 1 - x K_1(x) \tag{4b}$$

$$I_o(x)\, K_1(x) + I_1(x)\, K_o(x) = \frac{1}{x}, \tag{4c}$$

we are now able to do the radial integral.

$$T_\infty(r) = \frac{\dot{Q}}{\pi\kappa} \sum_{m=1,3,5\ldots} \frac{\sin (m\pi h)/2L}{m a_m^2} \cdot \begin{cases} 1 - (2a_m R)\, K_1(2a_m R)\, I_o(2a_m r), & r < R \\ (2a_m R)\, I_1(2a_m R)\, K_o(2a_m r), & r > R \end{cases}$$

$$= \frac{16\,\dot{Q}}{\pi^3 \kappa} L^2 F(\beta, x), \tag{5}$$

JSEP where $x = \pi R/2L$, $\beta = r/R$, and

JSEP

$$F(\beta, x) = \sum_{m=1,3,5\ldots} \frac{\sin(m\pi h)/2L}{m^3} \cdot \begin{cases} 1 - (mx)\,K_1(mx)\,I_o(\beta mx), & r < R \\ (mx)\,I_1(mx)\,K_o(\beta mx), & r > R. \end{cases}$$

The approximation error for large but finite t is calculated by integrating (2) first over r', expanding $I_o\left(\frac{2rr'}{q}\right) \exp - \left(\frac{r^2 + r'^2}{q}\right)$ in a power series.

$$\Delta T(r,t) - T_\infty(r) = -\frac{\dot{Q}}{\pi\kappa} \int_{4\alpha t}^{\infty} dq \left(1 - e^{-(r^2+R^2)/q} \sum_{n=0}^{\infty} \frac{(r^2/q)^n}{n!} \sum_{k=0}^{n} \frac{(R^2/q)^k}{k!}\right)$$

$$\cdot \sum_{m=1,3,5\ldots} e^{-a_m^2 q} \frac{\sin(m\pi h)/2L}{m}$$

$$= \frac{-\dot{Q}}{\pi\kappa} \int_{4\alpha t}^{\infty} dq \frac{R^2}{q} \left[1 - \frac{\left(\frac{R^2}{2} + r^2\right)}{q} + \ldots\right] \sum_{m=1,3,5\ldots} e^{-a_m^2 q} \frac{\sin(m\pi h)/2L}{m}$$

$$= \frac{-\dot{Q}L^2}{\left(\frac{\pi^3}{16}\right)\kappa} \sum_{m=1,3,5\ldots} \frac{\sin(m\pi h)/2L}{m^3} \left(\frac{R^2}{4\alpha t}\right) e^{-4\alpha t a_m^2}$$

$$\cdot \left[1 - \frac{\left(\frac{R^2}{2} + r^2 + \frac{1}{a_m^2}\right)}{4\alpha t} + \ldots\right]. \tag{6}$$

This error rapidly approaches zero when $4\alpha t \gg r^2$, R^2, and L^2. In a typical case, $L \sim R \sim 2\ \mu m$, $\alpha \sim 10^{-3}\ cm^2/s$ and the characteristic thermal diffusion time τ is 10 μs. For a heat pulse of duration $t \gg \tau$, we thus consider the temperature rise response to be a square wave of height T_∞ and duration t.

The family of universal curves $F(\beta, x)$ has been evaluated on a computer and is shown in Figs. I-11 and I-12. For small values of x, corresponding to rod-shaped irradiation volumes ($R \ll L$), the function F drops off sharply because of radial conduction as x is made smaller. For large x, corresponding to disk-shaped volumes ($R \gg L$), F approaches 1, but for small values of R the corresponding smaller value of L must be even smaller. This limits the temperature rise, by conduction to the temperature-clamped substrate. The net effect is illustrated in Fig. I-13, which shows the curves of constant L^2F on axis ($\beta = 0$) for penetrating beams ($h = L$) as a function of R and L. It is clear that for any given beam radius R, the requisite power density $\dot{Q}$ to achieve a

JSEP

JSEP

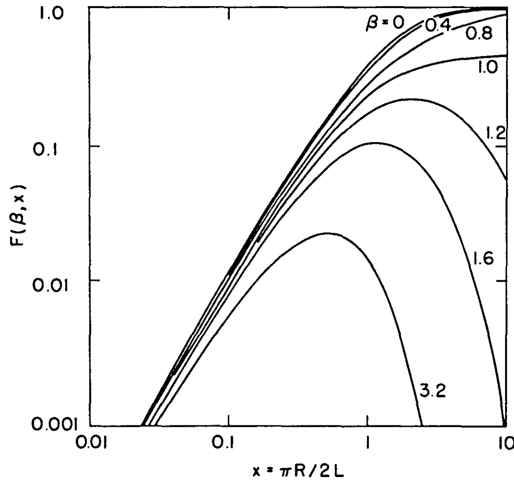

Fig. I-11.
F(β, x) for penetrating beams (h = L).

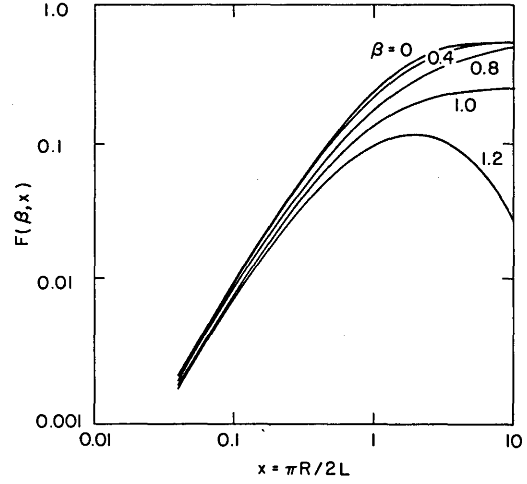

Fig. I-12.
F(β,x) for h = L/3. The region x < .25 may be physically inaccessible.

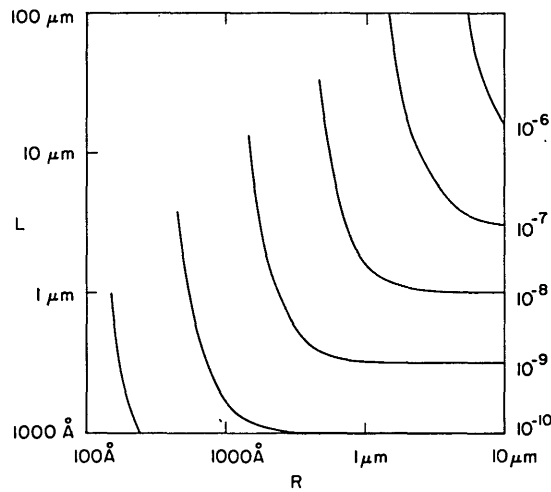

Fig. I-13. Curves of constant $L^2F(0, x)$ as a function of R, L for fully penetrating beams. Units in cm^2.

JSEP

JSEP

given temperature rise does not decrease appreciably as the specimen is made thicker than $L \approx R$. Nor does $\dot{Q}$ decrease very much if, for a given sample thickness L, the beam is made broader than $R \approx L$. Thus, in some sense, an irradiation volume in which $R \approx L$ is optimal.

2. Temperature Required for Thermal Desorption

The required temperture rise is determined by the binding energy E of the molecule of interest. The mean desorption lifetime τ is

$$\tau = \tau_o e^{E/kT}, \tag{7}$$

where the pre-exponential factor τ_o is usually taken to be 10^{-13} s, although it may be quite a bit different, or even a weak function of E.[4] In any case, the fraction f of molecules remaining adsorbed after a time t at temperature T is

$$f = e^{-t/\tau(T)}. \tag{8}$$

In order for a significant fraction to be desorbed ($f \sim 1/e$),

$$\tau(T) \approx t, \tag{9}$$

which implies

$$\frac{E}{kT} \approx \ln \frac{t}{\tau_o}. \tag{10}$$

When every picture element in a 256×256 frame is to be examined, t must be less than 10^{-1} s if the frame time is not to be excessive. Alternatively, a rapid scan could find a few elements to be examined subsequently with $t \sim 10^2$ s. As T varies with the log of t, E/kT is approximately 30 in either case, if $\tau_o = 10^{-13}$ s. This means, for example, that T must be ~300°K to desorb water from protein (15 kcal/mol), and 800°K to desorb sodium and potassium from blood. The required temperature rise ΔT is less than this, since the substrate temperature T_o may be varied. It must not, obviously, be so warm as to desorb a significant amount during the course of a scan. This means, for a frame with N^2 elements,

$$N^2 \tau(T) \ll \tau(T_o) \tag{11}$$

or

$$\ln N^2 < \frac{E}{k}\left(\frac{1}{T_o} - \frac{1}{T}\right) = \frac{E\Delta T}{kTT_o} \approx \ln \frac{t}{\tau_o} \frac{\Delta T}{T_o}. \tag{12}$$

For $t = 10^{-2}$ s, $\tau_o = 10^{-13}$ s, $N = 256$,

JSEP

JSEP

$$\frac{\Delta T}{T_o} > .44, \quad (13)$$

so $\frac{T_o}{T} < .70$, in order that the sample not be depleted by evaporation at the substrate temperature over the course of a run. This means that a temperature rise of at least 100°C is required to detect water on protein, or 260°C to detect alkalis from blood, with spatial resolution.

3. Electron-Beam Requirements

The heat generated by the electron beam within the sample is caused by small-angle inelastic electron-electron scattering. A single "depth-dose function" $\Lambda(f)$ has been found to be valid for low Z elements.[5] This function gives in turn the specific energy loss per unit depth penetration.

$$\frac{dV}{dz} = \frac{V_o}{R_G} \Lambda(f), \quad (14)$$

where $f = \frac{L - z}{R_G}$, $R_G = \left(\frac{.046}{\rho}\right) V_o^{1.75}$ μm, with V_o the beam voltage in kV, and ρ the target density in gm/cm^3. The Grun range R_G in biological material is typically 0.8 μm for 5 kV electrons, 2.6 μm for 10 kV. The function $\Lambda(f)$ is roughly an offset Gaussian in shape, with a peak value of 1.4 at $f = .33$ and a full-width at half-maximum of $\Delta f = .8$. In the spot-heat calculation, Λ was taken to be a constant equal to 1.0 for $f < 1.0$, and zero elsewhere. This is seen to be a reasonably good approximation, especially near the surface $(f = 0)$. The power density $\dot{Q}$, then, is given by

$$\dot{Q} = \frac{JV_o}{R_G}, \quad (15)$$

where J is the current density.

The transverse scattering is difficult to calculate, but experimental results in electron-beam lithography indicate that minimum linewidths are close to R_D, the diffusion range.[6] The diffusion range is roughly proportional to voltage V_o,

$$\frac{R_D}{V_o} \approx 0.2 \ \mu m/kV \quad \text{for} \quad \rho = 1. \quad (16)$$

Thus small values of x in the spot-heat calculation may be physically impossible unless $R_G \gg L$, in which case the beam loses only a small portion of its energy in the sample.

To return to the spot-heat calculation, the required current density in the electron beam may be estimated. From Fig. I-13, for R = 1 μm and L = 1.6 μm, $L^2F(0, x) = 10^{-8}$ cm^2. At 10 kV, for a temperature rise of 100°C, under the assumption that

JSEP

JSEP

$\kappa = .002$ W/cm-deg,

$$\Delta T = \frac{JV_o}{\left(\frac{\pi^3}{16}\right)\kappa R_G} L^2F(0,x), \tag{17}$$

and so

$$J = \frac{100 \times .004 \times 2.6 \times 10^{-4}}{1.0 \times 10^4 \times 10^{-8}} = 1 \text{ A/cm}^2. \tag{18}$$

For R = 1000 Å and L = 1 μm, $L^2F = 3 \times 10^{-10}$ cm^2, so J becomes 30 A/cm^2 at 10 kV. And for R = 150 Å and L = 5000 Å, $L^2F = 10^{-11}$ cm^2, so J jumps to 1000 A/cm^2.

It is not possible even in principle to increase J indefinitely by demagnification. The maximum current density J_m at the specimen is related to the cathode current density J_c by Liouville's theorem:[7]

$$J_m = J_c \frac{eV_o}{kT} (1 + \sin^2 \alpha), \tag{19}$$

where α is the half-angle subtended by the beam in image space and T the filament temperature. Spherical aberration requires that α be kept as small as possible, 10^{-3} to 10^{-2} in typical electron microscopes. Thus $J_m \gtrsim 10\ J_c$ for thermionic cathodes. Researchers in electron probe microanalysis[8] have found a practical limit to be 1 μA into a 1-μm spot at 30 kV, or J = 100 A/cm^2. Figure I-14, based on Broers and

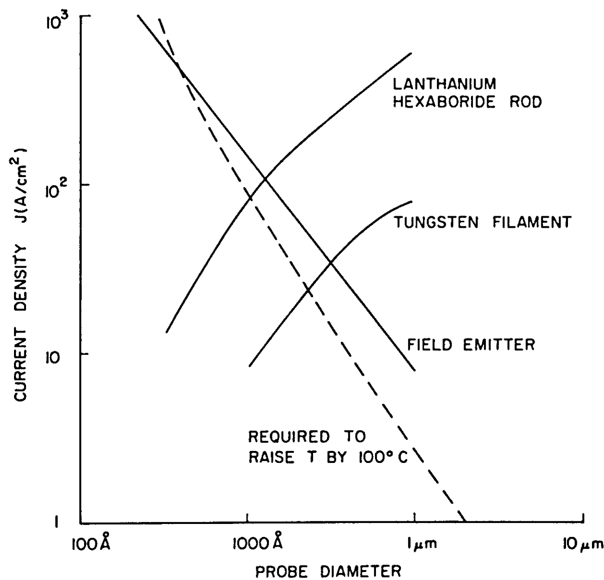

Fig. I-14. Electron beam current density vs probe diameter.

JSEP

JSEP Hatzakis,[9] shows current density as a function of probe diameter for thermionic tungsten and lanthanum hexaboride cathodes, and for field-emitting cathodes. This graph also shows the current density that is needed to raise the temperature of biological material ($\rho = 1$, $\kappa = 2 \times 10^{-3}$ W/cm-deg) by 100°C. For spots larger than 1000 Å, thermionic guns should be adequate. For finer spots, field-emitting guns are brighter and may possess the requisite power down to nearly 100 Å.

4. Measurement of Temperature Rise

Reimer and Christenhusz[10] have discussed ways of measuring the specimen temperature in an electron microscope. These methods include thin-film thermocouples, diffraction pattern changes caused by thermal expansion or melting, and irreversible changes, such as melting or evaporation, which are seen in electron image. Using the last of these, they measured as a function of beam diameter the current needed at 80 kV to melt an indium film, 380 Å thick, at the center of a 400 Å supporting film of SiO stretched over a 70 μm aperture in the Siemens Elmiskop I. The data agreed well with their theoretical formula (rewritten in the notation of this paper), which for relatively large-aperture radius r_o becomes

$$T_\infty(0) \approx \frac{\dot{Q}}{2\kappa} R^2 \left[\ln\left(\frac{r_o}{R}\right) + .29\right]. \tag{20}$$

This might be compared with the geometry of this paper when $R \ll L$, so radial conduction predominates. In this case ($x \ll 1$), we see from Fig. I-11,

$$F(0, x) \approx 1.5\, x^{7/4}, \tag{21}$$

and so

$$T_\infty(0) \approx \frac{\dot{Q}R^2}{2\kappa} \left[4 \left(\frac{2L}{\pi R}\right)^{1/4}\right]. \tag{22}$$

Both (20) and (22) have $\dot{Q}R^2/2\kappa$ multiplied by a slowly decreasing function of R, so the general behavior at least of the spot-heat calculation has been demonstrated in one case.

In practice the most uncertain parameters in the calculation are the thermal conductivity of the specimen, and perhaps L, the specimen thickness. For scanning desorption molecule microscopy of biological cells and tissue, the measurement of specimen temperature may be impossible to achieve with any of the methods listed. Fortunately, the desorption signal itself might be used as a thermometer, by measuring the velocity distribution of the desorbed neutrals. Once the relevant binding energies are known, the amount of desorption signal for given beam parameters should suffice

JSEP to estimate the temperature.

References

1. J. C. Weaver and J. G. King, Proc. Nat. Acad. Sci. USA 70, 2781 (1973).
2. H. S. Carslaw and J. C. Jaeger, Conduction of Heat in Solids (Oxford University Press, London, 2d ed., 1959), p. 373.
3. Ibid., p. 495.
4. L. A. Petermann, Nuovo Cimento Suppl. 5, 364 (1967).
5. T. E. Everhart and P. H. Hoff, J. Appl. Phys. 42, 5837 (1971).
6. R. D. Heidenreich et al., J. Appl. Phys. 44, 4039 (1973).
7. J. R. Pierce, Theory and Design of Electron Beams (D. Van Nostrand Co., Inc., New York, 1954), p. 116.
8. T. A. Hall, in G. Oster (Ed.), Physical Techniques in Biological Research, Vol. 1, Pt. A (Academic Press, Inc., New York, 1971), p. 157.
9. A. N. Broers and M. Hatzakis, Sci. Am., Vol. 227, No. 5, pp. 34-44, November 1972.
10. L. Reimer and R. Christenhusz, Lab. Invest. 14, 1158 (1965).

JSEP

JSEP